ISSN 1063-7710, Acoustical Physics, 2020, Vol. 66, No. 4, pp. 352–361. © Pleiades Publishing, Ltd., 2020.
Russian Text © The Author(s), 2020, published in Akusticheskii Zhurnal, 2020, Vol. 66, No. 4, pp. 366–376.

Designing Fully Populated Phased Arrays for Noninvasive Ultrasound Surgery with Controlled Degree of Irregularity in the Arrangement of Elements

P. B. Rosnitskiy[a], *, O. A. Sapozhnikov[a], L. R. Gavrilov[b], **, and V. A. Khokhlova[a]

[a]*Physics Faculty, Moscow State University, Moscow, 119991 Russia*
[b]*Andreyev Acoustics Institute, Moscow, 117036 Russia*
**e-mail: pavrosni@yandex.ru*
***e-mail: gavrilov.1938@mail.ru*

Received November 26, 2019; revised November 26, 2019; accepted February 25, 2020

Abstract—When designing phased antenna arrays for use in noninvasive ultrasound surgery, it is desirable to provide the highest possible power for a given array dimensions. At the same time, it is necessary to take into account the limitations on the maximum allowable ultrasound intensity at the array elements and to ensure suppression of spurious diffraction maxima in the spatial structure of the emitted field. The problem can be solved by designing an irregular arrangement combined with the densest filling of the array surface with elements. This paper presents a modification of such a method for creating fully populated arrays with nonperiodic tessellation distribution of elements, based on the restriction of the relaxation mechanism in an iterative array design algorithm. A computer model that allows for controlling the degree of irregularity in distribution of the array elements was developed. The stability of maintaining the low level of acoustic intensity in unwanted grating lobes was tested for various random realizations of the element arrangements by analyzing a statistical ensemble of 500 model arrays. The advantages of the considered arrays in comparison with existing models of fully populated arrays are demonstrated.

Keywords: medical acoustics, high-intensity focused ultrasound, multielement arrays, Rayleigh integral

DOI: 10.1134/S1063771020040090

INTRODUCTION

Multielement phased arrays [1, 2] with radiating elements situated on a spherical segment [3, 4] are currently widely employed in noninvasive high-intensity focused ultrasound (HIFU) surgery. The key requirement for many clinical applications is to provide high acoustic power of the array, which is sufficient to reach focal intensity levels necessary for a surgical operation. For example, an ultrasound beam suffers substantial power loss in transcranial irradiation of the brain [5–7] or in the treatment of deep-seated pancreatic tumors [8]. Such losses can be compensated by increasing the total power of the array. In this case, the key limitation is a maximum technically allowable intensity of about 30–40 W/cm^2 at the piezoelectric elements [4, 9, 10]. Given this limitation, one of the main approaches to increasing acoustic power of an array is to increase its active (radiating) surface, i.e., to maximize the filling factor of the array $\Psi = (\Sigma_{act}/\Sigma) \times 100\%$, where Σ_{act} is the total area of all radiating elements and Σ is the total area of the array surface. When developing an array model, one should also consider the need of a non-periodic arrangement of elements on the array surface for suppressing grating lobes formed by electronic steering of the focus [11–13]. In addition, individual elements must be of equal area since differences in their areas complicates matching the outputs of power amplifiers with the elements and deteriorates the characteristics the acoustic field when electronically steering of the focus.

In the last decade, various attempts have been made to increase the filling factor of arrays by arranging the elements in tessellations with different tilings. The authors of [14] proposed two array configurations based on the Penrose rhombus tiling (filling factor of about Ψ = 70% with 0.5 mm gaps between the elements) and on non-periodically arranged rectangular elements (Ψ = 71% with 0.5 mm gaps) (Figs. 1a and 1b, respectively). Recently, an array model with elements shaped as Voronoi tessellation cells and arranged following the pattern of Fermat's spiral was proposed [15]. Such array has a filling factor of about Ψ = 78% with 0.5 mm gaps between the elements (Fig. 1c). Hence, in English literature, this array was named a Voronoi Tessellation Fermat's Spiral array (VTFS array). Such arrays are already used in practice

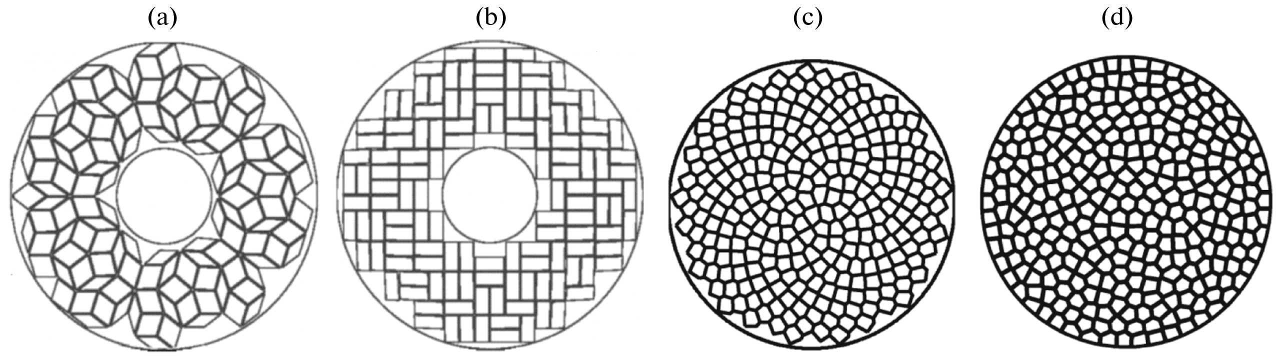

Fig. 1. Sketches of arrays with various tessellation filling by elements: (a) Penrose tiling, (b) rectangular tiling, (c) Voronoi tessellation Fermat's spiral array, and (d) fully populated tiling with cells of equal area.

[16]. Despite the dense pattern of VTFS array elements, its geometry does not yield the maximum possible filling factor due to unfilled areas at the periphery of the transducer (Fig. 1c). Furthermore, the polygonal cells of the Voronoi tessellation used in the array construction have different areas. The dashed curve in Fig. 2 shows the dependence of the cell area Σ_{cell} on its number n, where the numbers are ordered as the distance between the center of mass of the cell and the center of the array increases. The maximum difference between the cell areas is 19% of the mean cell area, whereas most strong differences are observed for the central cells.

In 2018 the authors of the current paper proposed a novel type of tessellation arrays with maximum possible filling factor ($\Psi = 100\%$ if the area of technological gaps between the elements is negligible), i.e., the fully populated arrays (Fig. 1d) [17]. The proposed model was based on the concept of random elements arrangement (randomization) [11, 18], the capacity-constrained tessellation was used as a pattern, and equal areas of the elements were achieved with a specific algorithm described in [19].

The dispersion in the cell areas of the two densely packed arrays, which are the VTFS array [15] and the proposed fully populated array with elements shaped as the capacity-constrained tessellation cells, is compared in Fig. 2 [17]. Both arrays have the same outer contour and mean cell area (Figs. 1c, 1d). Due to the absence of empty boundary elements, the number of elements in the second array (291) exceeds the number of elements in the first one (256). The element areas of the fully populated array are shown in Fig. 2 by a solid curve, and the element areas of the VTFS array by a dashed curve. Note that the algorithm of the capacity-constrained tessellation is numerical; therefore, the equality of the element areas is approximate: the maximum difference between the cell areas is 2.8% of the mean cell area. If necessary, this difference can be decreased to the required level by increasing the number of points in the tessellation algorithm (see below). In contrast to the capacity-constrained tessellation, the VTFS array has a considerably larger dispersion in the element areas, especially far from the edge of the array. For the example considered here, the maximum deviation of the element area from the mean value is 19%.

Despite the fact that the elements of such fully populated arrays are arranged in a random manner, the periphery layer of cells at the outer boundary is inevi-

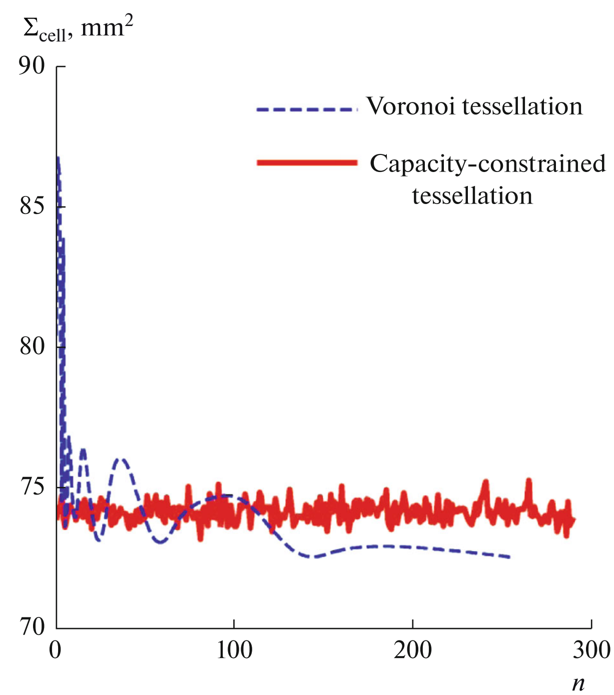

Fig. 2. Dependence of cell area Σ_{cell} on its number n for partitioning of the array surface by cells of VTFS tessellation (dashed curve) and by capacity-constrained tessellation (solid curve). Both tessellations have the same mean cell area of 74 mm^2 and are constructed on a spherical segment with radius of curvature F = 160 mm and aperture D = 160 mm. Cell numbers n are ordered in accordance with distance of their center of mass from the center of the array.

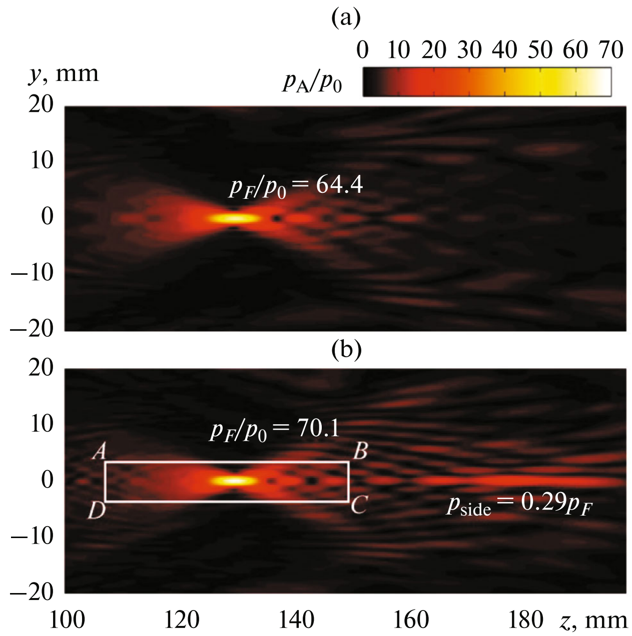

Fig. 3. Two-dimensional distributions of normalized amplitude of acoustic pressure p_A/p_0 in array axial plane *zy*: (a) for existing VTFS array and (b) for fully populated array. In both distributions, dimensionless values of focal amplitude p_F/p_0 are indicated above the focal region. Amplitude p_{side}/p_F in the most intensive sidelobe located outside rectangular focus vicinity ABCD are shown for the distribution (b). The longitudinal dimension and location of contour ABCD were selected so that it contains two axially located prefocal and two postfocal lobes. Similarly, transverse boundary of the rectangle satisfies condition that ABCD region contains two side grating lobes at both sides.

tably quasi-annular; therefore, these periphery layers also line up into an annular-like structure. The effect of such partial regularity of the element arrangement is almost negligible for arrays with a large number of elements ($N > 256$); however, it can be noticeably stronger for arrays with smaller number of elements. As an illustration of this side effect, distributions of the dimensionless pressure amplitude p_A/p_0 are plotted in the *zy* plane ($x = 0$), which passes through the array axis z (Fig. 3). Here, p_0 is the pressure at the element surface; x and y are the axes of the rectangular coordinate system in a plane perpendicular to the z axis of the array, with the origin at its center of symmetry. The distributions for the VTFS array (Fig. 3a) are compared to the fully populated one (Fig. 3b). When the focus is shifted by 30 mm from the center of curvature ($F = 160$ mm) of the arrays along the z axis toward the array surface, the grating lobes at the axis of the VTSF array without annular periodicity almost do not appear, whereas the side lobes are clearly seen at the axis of the fully populated array.

The objective of this work was to develop a modification of the method for designing fully populated random arrays that would suppress the effect of periodicity in element arrangement and decrease the corresponding level of grating lobes that form with electronically steering the array focus.

THEORETICAL MODEL

The proposed modification for constructing a fully populated array was implemented in a step-by-step procedure, the first part of which was the same as in the recently proposed method [17]. To illustrate the sequence of operations for the existing method, the example of constructing a four-element array in the form of a spherical segment is presented first:

(1) The surface of the array is filled with a large number of sampling points, which are randomly generated over its surface with uniform distribution over a solid angle (Fig. 4a). In other words, the probability that a random point belongs to an element area $d\Sigma$ at the array surface of total area Σ is defined as $d\Sigma/\Sigma$ and does not depend on the position of the element on the sphere.

(2) All points are divided into N classes containing an equal number of points M (Fig. 4a). The division of the points into classes occurs randomly, therefore the “point clouds” of different classes are strongly mixed, and each cloud densely “covers” the entire surface of the array. This initial state is considered as the zero iteration $S = 0$. In this example, $N = 4$, $M = 250$, and the total number of points is $NM = 10^3$. The points of four different clouds are depicted by different types of markers in Fig. 4a (plus signs, circles, dots, and squares).

(3) Next, the iteration process of pairwise separation of point clouds of different classes is implemented. It can be visualized as a separation of N different “immiscible liquids” mixed in a two-dimensional “container.” Each liquid consists of the same number of particles M, tending to join each other and to form compact cells. The final state after separation of such “liquids” (Fig. 4b) will correspond to partitioning the volume of the “container”, i.e. the array surface, into equal-sized cells. Separation occurs as follows. For each iteration S, all possible pairs of point clouds of different classes are considered. As an example, consider the clouds depicted with “+” and “o” markers in Fig. 4a. Denote the radius–vectors of the points in the first cloud at the Sth iteration as $\mathbf{a}_i^S$ ($i = 1, \ldots, M$). Introduce “the center of mass” of the cloud as

$$\mathbf{A}_S = \left(\mathbf{a}_1^S + \mathbf{a}_2^S + \ldots + \mathbf{a}_M^S\right)/M, \qquad (1)$$

where S is the iteration number. Similarly, for the second point cloud, the radius-vectors $\mathbf{b}_j^S$ and the corresponding center of mass $\mathbf{B}_S$ ($j = 1, \ldots, M$) are introduced. Note that in general, the centers of mass determined from Eq. (1) are not located at the spherical surface of the array. Therefore, an additional projec-

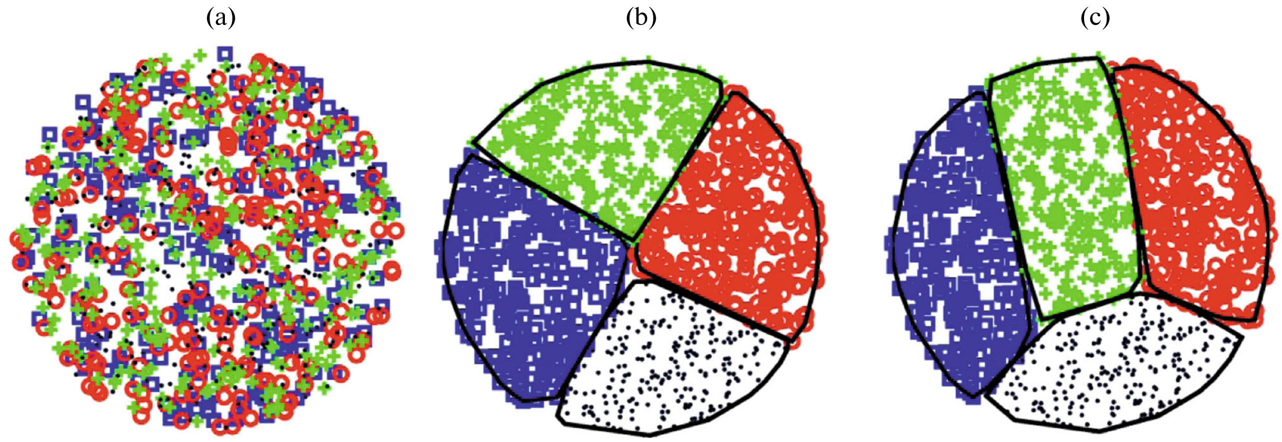

Fig. 4. Illustration of the capacity-constrained tessellation algorithm for 100% filling of array surface by equal-area polygonal elements for constructing four-element array. The points of corresponding clouds are depicted by different types of markers (plus sign, circle, point, and square). Initial location of points with full mixing (zero iteration) is shown at (a). Final result of dividing point clouds into cells is presented for two cases: (b) array without limitation of relaxation and (c) array with limitation of relaxation at the fifth iteration.

tion of the centers of mass to the array surface is performed along the normal to the surface and the obtained points are further considered as the centers of mass. To implement the process of separating point clouds, all possible pairs $(\mathbf{a}_i^S, \mathbf{b}_j^S)$ are considered. If the point $\mathbf{a}_i^S$ of the first cloud is located in the zone of influence of the center of mass of the second cloud (the corresponding criterion is given below) and the point $\mathbf{b}_j^S$ of the second cloud is located in the zone of influence of the center of mass of the first cloud, the points are exchanged. In this case, the point $\mathbf{b}_j^S$ is assigned to the first cloud and the point $\mathbf{a}_i^S$—to the second one. As a quantitative criterion, the following decision function was introduced in [19], which identifies pairs of points to be exchanged:

$$\chi\left(\mathbf{a}_i^S, \mathbf{b}_j^S, \mathbf{A}_S, \mathbf{B}_S\right) = \rho\left(\mathbf{a}_i^S, \mathbf{A}_S\right)^2 - \rho\left(\mathbf{a}_i^S, \mathbf{B}_S\right)^2 + \rho\left(\mathbf{b}_j^S, \mathbf{B}_S\right)^2 - \rho\left(\mathbf{b}_j^S, \mathbf{A}_S\right)^2. \tag{2}$$

Here, $\rho(\mathbf{X}, \mathbf{Y})$ is the distance between the two points in the spherical metric, or, in other words, the arc length of the great circle passing through the points $\mathbf{X}$ and $\mathbf{Y}$. If $\chi\left(\mathbf{a}_i^S, \mathbf{b}_j^S, \mathbf{A}_S, \mathbf{B}_S\right) > 0$, then the points are exchanged, otherwise no exchange occurs. Thus, the exchange between points of two clouds during the Sth iteration terminates after overrun of all possible pairs of points $(\mathbf{a}_i^S, \mathbf{b}_j^S)$. Then, the location of centers of mass of clouds is corrected using Eq. (1) and the same procedure is performed for all other possible pairs of clouds. For the pairs of clouds already considered, the condition (2) can be violated during the iteration, but on average, the clouds become more separated. The iteration process $S \to S+1 \to \ldots S_{\max}$ continues until the condition $\chi\left(\mathbf{a}_i^{S_{\max}}, \mathbf{b}_j^{S_{\max}}\right) \le 0$ is satisfied for all points from an arbitrary pair of clouds. Fulfillment of this condition indicates complete separation (Fig. 4b). It should be noted that after separation, each of the N clouds contains the same number of M points, since the exchange of points between the clouds has always been pairwise.

(4) In order to make the transition from a discrete representation of clouds to a continuous one, a convex rim is constructed surrounding the outer points of each cloud (Fig. 4b). In the case of a large number of sampling points, the resulting polygons are precisely tessellation cells, which fill the array surface without any gaps. In accordance with the algorithm, each cell contains the same number of M sampling points randomly generated and uniformly distributed over the sphere. Therefore, according to the Monte Carlo method, in the limit of a large number of points M, the areas of cells are equal.

The example in Fig. 4 shows that after building a tessellation of four elements, certain regularity (and periodicity) appears in the arrangement of cells: the construction performed actually led to the division of the spherical surface into four almost identical sectors (Fig. 4b).

To diminish the effect of periodicity, here it was proposed to modify the step 3 of the algorithm, namely, to change the decision-making function (2). Clearly, the decision function χ depends on both coordinates $\mathbf{a}_i^S$ and $\mathbf{b}_j^S$ of the sampling points and locations $\mathbf{A}_S$ and $\mathbf{B}_S$ of the centers of mass, whereas the arguments of the function are changed at each iteration. In this case, at each S-th iteration of partition, two separate processes occur. First, points are exchanged

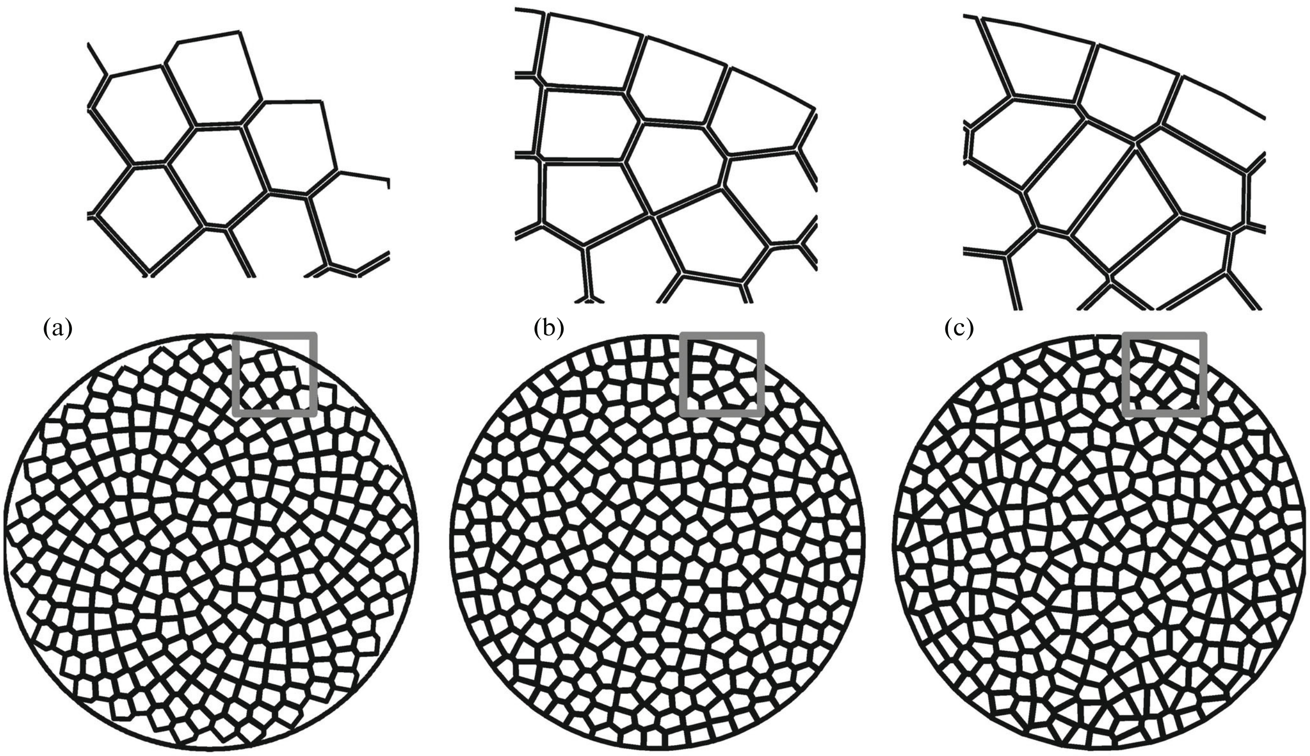

Fig. 5. Frontal view of arrays with different types of tessellation. All arrays are constrained by the same circular contour and have elements of equal averaged area: (a) 256-element VTFS array, (b) 291-element fully populated array without limitation of relaxation, (c) similar array with limitation of relaxation. Upper insets show enlarged images of several array elements to better illustrate element shape and gaps between them. The parameters of arrays are as follows: frequency $f = 1.2$ MHz, radius of curvature $F = 160$ mm, aperture $D = 160$ mm, gap between elements 0.5 mm, and mean area of each element 66 mm^2.

between clouds according to the condition $\chi\left(\mathbf{a}_i^S, \mathbf{b}_j^S, \mathbf{A}_S, \mathbf{B}_S\right) > 0$, which results in separation of the point clouds (future cells) among themselves. The second process is a displacement of the centers of mass $\mathbf{A}_S$ of each of the clouds at the end of the iteration (1), which moves the cloud as a whole, resulting in the final establishment of the equilibrium position at the last iteration, i.e., "relaxation". Namely, the process of relaxation of the center of mass leads to formation of cells similar to each other in shape and to periodicity in their final locations. Indeed, let the relaxation be limited at some iteration $S = S_0$, e.g., $S_0 = 5$. This means that at all iterations $S > S_0$, the centers $\mathbf{A}_S$ and $\mathbf{B}_S$ for any pair of point clouds will be fixed at locations $\mathbf{A}_S = \mathbf{A}_{S_0}$, $\mathbf{B}_S = \mathbf{B}_{S_0}$. The new decision-making function will look as follows:

$$\tilde{\chi}\left(\mathbf{a}_i^S, \mathbf{b}_j^S, \mathbf{A}_S, \mathbf{B}_S\right) = \begin{cases} \chi\left(\mathbf{a}_i^S, \mathbf{b}_j^S, \mathbf{A}_S, \mathbf{B}_S\right), & S \le S_0, \\ \chi\left(\mathbf{a}_i^S, \mathbf{b}_j^S, \mathbf{A}_{S_0}, \mathbf{B}_{S_0}\right), & S > S_0. \end{cases} \quad (3)$$

This change allows for considerable reduction in periodicity: the final pattern is spatially more nonuniform (Fig. 4c) and the cells are more different in shape from each other. It is important to note that this construction fulfills the condition of equal areas, since the exchange of points between clouds remains pairwise as before.

Consider the influence of the introduced limitation of relaxation on the array capabilities of electronic steering the focus. Compare the 256-element VTFS array (Fig. 5a) [15], the fully populated array with cells of a given area without limitation of relaxation (Fig. 5b) [17], and the fully populated array with limited relaxation proposed here (Fig. 5c). For a proper comparison, the same array parameters were chosen, which correspond to the existing VTFS array: the operating frequency is 1.2 MHz, the radius of curvature is $F = 160$ mm, and the aperture is $D = 160$ mm. For all types of arrays, the same average area of the elements was chosen and the same technological gaps between the adjacent sides of neighboring elements (0.5 mm) were introduced, which in practice allows for avoiding electrical breakdown between the elements (Fig. 5, top insets) [3, 4, 16].

Both models of fully populated arrays were constructed using the same number of sampling points $M = 5 \times 10^5$ per element. When constructing the fully populated array with limited relaxation, this restriction was applied on the 8th iteration ($S_0 = 8$). To validate the method reliability, 500 such models of fully populated arrays were constructed with various initial distributions of mixing points generated in a pseudo-random manner.

For detail evaluation of dynamic focusing capabilities of the three arrays (Fig. 5), a series of calculations was performed with electronic focus steering of the existing and proposed arrays to the nodes of a certain grid in the axial plane zy ($x = 0$ mm). The same amplitudes of the normal velocity at the surface of the array elements were considered; the focus was steered by changing the velocity phase that was calculated along the rays connecting the centers of mass of each element and the focus point. For each focus location $(x_F = 0, y_F, z_F)$, the distributions of pressure amplitude $p_A(x, y, z)$ were calculated, and two parameters of the field quality, "efficiency" and "safety" of irradiation, were automatically analyzed. In accordance with the criteria introduced in earlier studies [13, 20], sonication is considered efficient if the intensity at the steered focus is higher than 50% of the maximum achievable value, and sonication is considered safe if the intensity of the grating lobes is less than 10% of the intensity in the steered focus. For analyzing the efficiency of sonication, the focus was steered in the axial plane over a rectangular grid with spatial windows of $110\text{ mm} \le z_F \le 200\text{ mm}$ and $-20\text{ mm} \le y_F \le 20\text{ mm}$, and steps of $\Delta z_F = \Delta y_F = 0.25$ mm. As analyzing the safety of sonication required a larger number of operations; a rougher grid steps of $\Delta z_F = \Delta y_F = 2.5$ mm were chosen, and the spatial windows of $110\text{ mm} \le z \le 200\text{ mm}$ and $-20\text{ mm} \le y \le 20\text{ mm}$ were kept the same for each focus location $(x_F = 0, y_F, z_F)$. Therefore, the array field had to be calculated 629 times.

The considered ultrasound arrays are composed of spherical polygon-shaped elements as illustrated in Fig. 5. To calculate the fields generated by these arrays, an analytical method based on the calculation of the Rayleigh integral was used:

$$p_A(\mathbf{r}) = -\frac{i\omega\rho_0}{2\pi}\int_{\Sigma}\frac{v_n(\mathbf{r}')\exp(ikR)}{R}d\Sigma'. \qquad (4)$$

Here, p_A is the complex pressure amplitude at the point $\mathbf{r}$ for a harmonic wave with a time dependence described as $\exp(-i\omega t)$, i is the imaginary unit, $\omega = 2\pi f$ is the angular frequency of the array, $k = \omega/c_0$ is the wavenumber, c_0 is the ultrasound speed, ρ_0 is the ambient density of the medium, Σ is the active surface area of the array, $v_n(\mathbf{r}')$ is the amplitude of the normal component of the velocity at point $\mathbf{r}'$ on the array surface, $d\Sigma'$ is the surface element with the center at the indicated point, and $R = |\mathbf{r} - \mathbf{r}'|$ is the distance from the indicated surface element to the observation point.

The integral (4) was calculated for each array element using the far-field approximation [13, 17]. Each polygon-shaped element of the array oscillating in a piston-like manner with the normal velocity amplitude v_0 was divided into right triangle-shaped subelements. Since the characteristic diameter of the subelements is much smaller than the array's radius of curvature F, the field of each subelement can be approximated by an analytical solution for its far field already at small distances from the array [17]:

$$p_A = \frac{p_0 ab\exp(ikr_0)[I(a,x) - I(b,y)]}{2\pi r_0(ax/r_0 - by/r_0)}. \qquad (5)$$

Here $I(a,x) = \exp(-ikax/2r_0)\operatorname{sinc}(kax/2r_0)$, a and b are the legs of the right triangle, $p_0 = \rho_0 c_0 v_0$ is the characteristic pressure at the surface of the element, $r_0 = \sqrt{x^2 + y^2 + z^2}$, and (x, y, z) are the coordinates of the observation point. The field of each element therefore was calculated analytically as the sum of the fields (5) of its subelements. It has been previously shown that such analytical method allows for accelerating the field calculation by several orders of magnitude in comparison with direct numerical calculation of the integral (4) [13, 17].

RESULTS

With the introduction of a technological gap of 0.5 mm, the filling factor of the array surface decreases from 87 to 78% for the VTFS array and from 100 to 89% for the fully populated arrays. For the VTFS array with 256 elements, the mean area of elements, taking into account the gaps, was $\bar{\Sigma}_{el} = 66\text{ mm}^2$. Since fully populated arrays have no inactive regions on the periphery of their surface (Figs. 5b, 5c), for the same area of elements, their number increased to $N = 291$. With $M = 5 \times 10^5$ sampling points per element used in constructing fully populated arrays, a variation coefficient of their element areas was $\bar{\Sigma}_{el}/\sigma_{el} < 1\%$, which makes it possible to consider them as being equal. Here, σ_{el} is the standard deviation of the element area.

In the procedure of constructing the fully populated array with limited relaxation, the fixed number of iterations ($S_0 = 8$) was chosen from the following consideration. Prior to the iteration process, some point cloud, which finally formed an array element, was selected. The displacement of the center of mass $\Delta r_S = |\mathbf{A}_S - \mathbf{A}_{S-1}|$ of this cloud was observed at each iteration S with respect to the previous one. As depicted in Fig. 6, starting from $S = 5$, the location of the center of mass varies insignificantly ($\Delta r_S < 0.5$ mm) slightly oscillating up to the last iteration. In other words, the locations of the centers of mass of elements are mainly settled at early iterations, and the subsequent elements only change shape, without changing their location, becoming increasingly

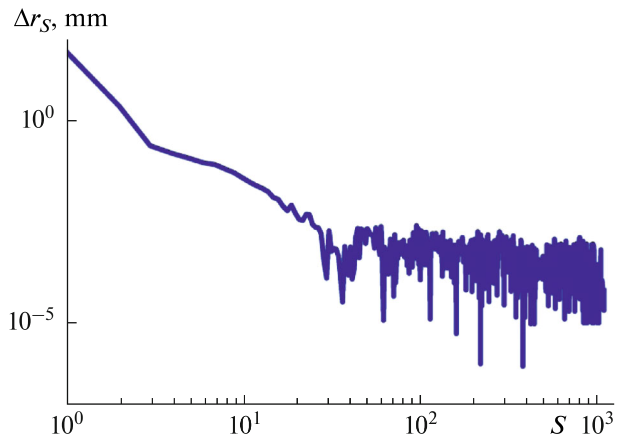

Fig. 6. Typical dependence of shift $\Delta r_S = |\mathbf{A}_S - \mathbf{A}_{S-1}|$ of center of cell mass on iteration number S for construction of tessellation with elements of equal area without limitation of relaxation. Here, $\mathbf{A}_S$ is radius vector of cell center of mass at Sth iteration. For convenience, the results are presented in logarithmic scale on both axes.

rounded up to the last iteration (Figs. 5b, 5c). The limitation of relaxation thus can be set at any iteration starting from $S = 5$, and the sooner this is done, the more elongated the final elements will be. When constructing the fully populated array with limitation of relaxation considered here, the limitation was set at iteration $S_0 = 8$ to avoid extreme elongation of the array elements.

First, compare the sketches of the arrays. Indeed, the limitation of relaxation allows for considerable weakening the regularity in the shape and arrangement of the array elements (Fig. 5c) compared to the case of no limitation of relaxation (Fig. 5b): the elements are slightly more asymmetric and randomly oriented. To assess the degree of elongation of the elements, the following factor: $\kappa = \bar{\Pi}_{\text{el}}^2/4\pi\bar{\Sigma}_{\text{el}}$ is introduced, where $\bar{\Pi}_{\text{el}}$ and $\bar{\Sigma}_{\text{el}}$ are the mean perimeter and area of the element. For a circular element shape, which is the most compact compared to other element shapes, $\bar{\Pi}_{\text{el}}^2 = 4\pi\bar{\Sigma}_{\text{el}}$, i.e., $\kappa = 1$. For elongated elements $\kappa > 1$, and the stronger the element is elongated, the greater is the value of κ. For the VTFS array, the array without limitation of relaxation, and the array with limitation by $S_0 = 8$, these factors are 1.173, 1.168, and 1.258, respectively.

Now compare the fields generated by these three arrays. First, consider the case of focusing at the center of curvature $F = 160$ mm, when all the elements of the arrays work in phase. Figure 7a shows the distributions of the pressure amplitude p_{A}/p_0 on the array axis z normalized to the initial pressure p_0 for the VTFS array (thick solid curve) and two fully populated arrays without limitation of relaxation (dashed curve) and with limitation of relaxation (thin solid curve). These distributions show that the normalized pressure amplitude at the focus of the VTFS array is $p_F/p_0 = 83$, whereas for the two fully populated arrays, it is 13% larger: $p_F/p_0 = 94$. Hence, the fully populated arrays allow achieving a 28% higher focal intensity, which corresponds to the ratio of the effective areas or the number of array elements. Here, we use the relations that $I \sim p_{\text{A}}^2, I_F \sim \Sigma_{\text{act}}^2$.

To demonstrate the degree of randomness of element arrangement, steering of the focus toward the array surface by 30 mm along the beam axis ($x_F = 0$ mm, $y_F = 0$ mm, $z_F = 130$ mm) was analyzed. The amplitude distributions (Fig. 7b) show two side effects related to the discrete structure of the arrays. The focal pressure amplitude decreases compared with the case without electronic steering (decrease in efficiency); behind the focus, a region of grating lobes forms (decrease in safety). As a quantitative estimate of the grating lobe amplitude, maximum field amplitude p_{side}/p_F beyond the focal maximum and first two adjacent lobes (Fig. 3b, contour line ABCD) were introduced. The results indicate that the amplitude of grating lobes for the fully populated array with limitation of relaxation (Fig. 7b, thin solid curve, $p_{\text{side}}/p_0 = 11.7$) is 48% less than for the fully populated array without limitation of relaxation (dashed curve, $p_{\text{side}}/p_0 = 22.4$). These results confirm the assumption of additional suppression of the regularity in the location of elements by limitation of relaxation. Even lower level of grating lobes ($p_{\text{side}}/p_0 = 8.7$) are achieved in the field of the VTFS array (thick solid curve). However, in this case, the amplitude in the steered focus is lower ($p_F/p_0 = 64$) than for the two fully populated arrays ($p_F/p_0 \approx 70$).

Figure 8 shows simulation results for electronic focus steering of the existing and proposed arrays into the nodes of a certain grid in the array's axial plane zy ($x = 0$ mm). The sonication efficiency and safety levels were analyzed for each focus location. The results are presented as contours of the regions of safe (the intensity of sidelobes does not exceed 10% of the focal intensity, thick curves) and efficient (the intensity in the shifted focus is higher by 50% of the maximum possible value, thin curves) focus steering in the axial plane yz. Dashed curves correspond to the contours for the VTFS array, and solid and dotted curves are contours for fully populated arrays with and without limitation of relaxation, respectively.

The region of safe focusing for the VTFS array (thick solid curve) clearly appears as the most elongated in the axial direction with a size along the z axis of about 87 mm. For the fully populated array without limitation of relaxation, this size along the z axis is considerably smaller, about 57 mm (thick dotted curve). The length of the mean safe focusing region for

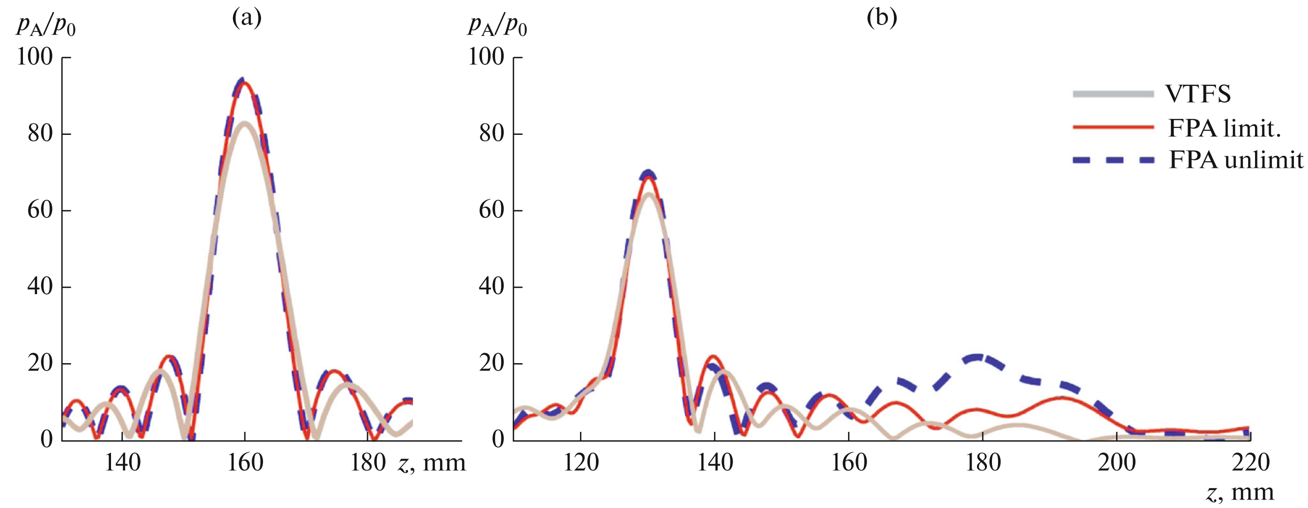

Fig. 7. Distributions of acoustic pressure amplitude p_A normalized to initial pressure p_0 along axis of symmetry of array (axis z) for (a) focusing to center of curvature and (b) electronic steering of focus along axis z by 30 mm toward array surface. Thick solid curve corresponds to VTFS array and thin solid and dashed curves correspond to fully populated arrays with limitation of relaxation and without it, respectively.

the fully populated array with limitation of relaxation is 76 mm (thick solid curve). The difference between the arrays in the length of safe focusing regions is reasonable and confirms the assumption on diminishing the annular structure of element arrangement via a transition from unlimited to limited relaxation. A decrease in the periodicity weakens the grating lobes; therefore, the length of the safe focusing region along the z axis increases. Note that regardless of the threshold of the limitation of relaxation, the outer elements of the fully populated array will always be located on its round boundary and form a ring. This explains the fact that the array with limitation of relaxation still has a safe focusing region 11 mm shorter than the VTFS array, which by design contains no annular structures. In the transverse direction along the y axis, all three arrays exhibit close sizes of safe transverse focusing regions ~35 mm in width with local deviations up to 2 mm.

The regions of efficient focusing (thin curves in Fig. 8) for all three arrays differ from each other less significantly than the regions of safe focusing. For the VTFS array (thin dashed curve) and fully populated array without limitation of relaxation (thin dotted curve), the sizes of these regions along the z and y axes are 58×22 and 56×21 mm, respectively. Corresponding dimensions for the fully populated array with limitation of relaxation are 55.5×20 mm along the z and y axes (thin solid curve), which is 1–2.5 mm smaller than for the other arrays. This slight difference in capabilities of effective steering for the VTFS array and fully populated arrays can be explained as follows: although the arrays have the same mean element area $\bar{\Sigma}_{el}$, the element areas in the VTFS array differ from each other more than the element areas of the fully populated arrays (Fig. 2). Moving away from the array center, the elements of the VTSF array become smaller and starting from the 110th element are smaller in area than the elements of the fully populated array. The peripheral elements of the VTFS array therefore are smaller in size and exhibit a wider directivity pattern, which yields a slightly larger region of efficient focusing along the axis z. Therefore, a small gain in the size of the efficient focusing region for the VTFS array is caused by variations in the area of its elements, which itself is a serious problem in array design. The fully populated array with limitation of relaxation exhibits the smallest efficient focusing region, since its

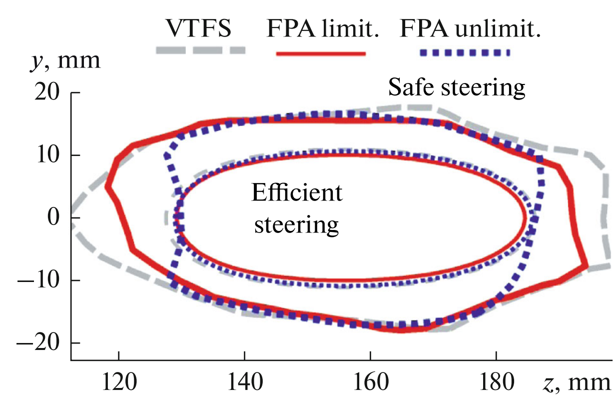

Fig. 8. Contours surrounding regions of efficient and safe electronic focus steering in axial plane zy. Focusing inside the contours can be considered efficient (thin curves) and safe (thick curves). Dashed curves correspond to VTFS array; solid and dotted curves correspond to fully populated arrays with and without limitation of relaxation, respectively.

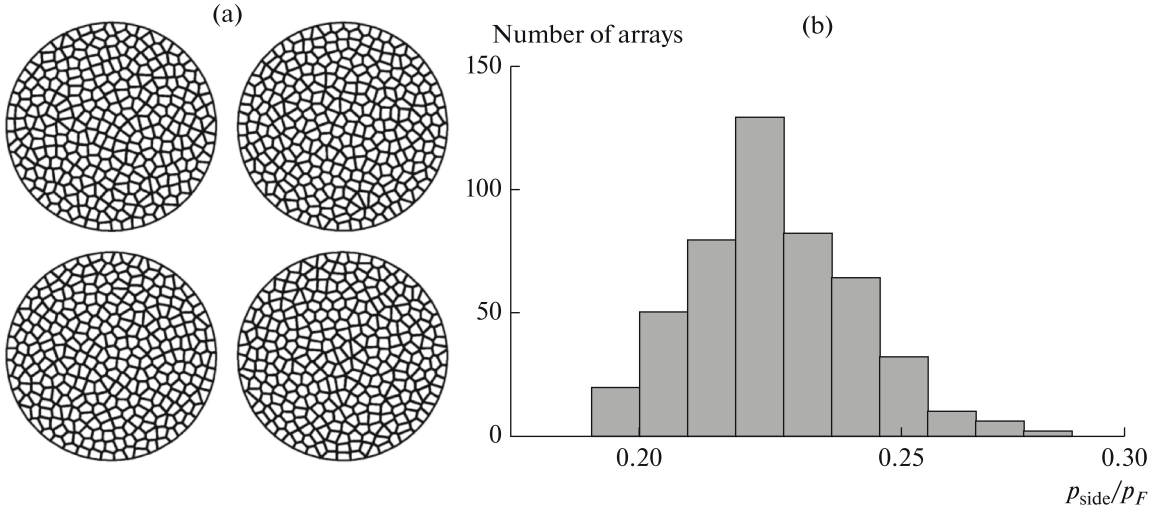

Fig. 9. (a) Examples of fully populated arrays with limitation of relaxation. The arrays have same parameters but various pseudorandom distributions of elements. (b) Histogram of distribution of 500 such arrays over amplitude p_{side} of grating lobe normalized to focal pressure amplitude p_F when steering the focus along axis z by 30 mm toward array surface. Parameters of all arrays are as follows: frequency $f = 1.2$ MHz, radius of curvature $F = 160$ mm, aperture $D = 160$ mm, gap between elements 0.5 mm, and mean area of each element 66 mm^2.

elements (Fig. 5c) are slightly more elongated compared to the other arrays. This is confirmed by values of factor κ, which describes the degree of elongation. The width of the directivity pattern for elements of the array with limitation of relaxation are slightly smaller, which leads to a slight decrease in the size of the region of efficient focusing.

Finally, simulation results for each array demonstrated that the region of both safe and efficient (i.e., "allowable") focus steering is determined by the efficient focusing region. Only for the fully populated array without limitation of relaxation the safe focusing region intersects that of the efficient focusing by 1 mm. Therefore, when developing arrays for practical purposes, relaxation limitation S_0 can be chosen in a broad range. With an increase of $S_0 > 8$, its value can be selected so that it yields the optimum degree of roundness of the elements, i.e., yielding an efficient focusing region close to the maximum possible size and locating it within the safe focusing region.

An important characteristic of the proposed method of limitation of relaxation is its application reliability for different realizations of a random distribution of elements over the array surface. Indeed, the algorithm for constructing the fully populated array has two sources of randomness: generation of a large number of points on its surface ($MN \sim 10^8$) and their subsequent separation into randomly mixed point clouds (Fig. 4a). The diagrams of four arrays as examples from the set of 500 arrays considered in this paper are shown in Fig. 9a. Since the location of elements influences the level of grating lobes when steering the focus electronically, the array fields are compared in terms of the degree of their manifestation. Figure 8 shows that the appearance of periodicity in element arrangement mainly influences the dimensions of steering at the array axis, where the contours of safe focusing region becomes closer to that of the efficient focusing (thick and thin dashed curves in Fig. 8). Therefore, a point of focus steering with coordinates $x_F = 0$ mm, $y_F = 0$ mm, and $z_F = 130$ mm, which is close to the boundary of the region of efficient steering of the focus, is chosen here to analyze a comparative parameter of the level of grating lobes with respect to normalized focal pressure amplitude p_{side}/p_F when steering the focus to this point.

The distribution of 500 arrays over the level of the parameter p_{side}/p_F is shown in the histogram divided into ten intervals of equal length (Fig. 9b). The height of each column corresponds to the number of arrays for which the parameter p_{side}/p_F falls into a given interval. It can be seen that the distribution of the random value p_{side}/p_F has a typical bell-shaped pattern. The level of grating lobes p_{side}/p_F is in the interval $0.19 \le p_{side}/p_F \le 0.29$, and the most frequently occurring level obtained for 129 of the 500 arrays lies in the interval $0.22 \le p_{side}/p_F \le 0.23$. It is important that the safe sonication condition is satisfied for all arrays. Nevertheless, this statistical analysis allows the selection of the best array realization shown in Fig. 5c with the minimum value of the parameter p_{side}/p_F.

CONCLUSIONS

In this work, a modification of the method for constructing fully populated arrays with a random distribution of radiating elements was proposed. A filling factor of such arrays is $\Psi = 100\%$ without introducing technological gaps between their elements. The proposed method allowed decreasing the level of grating lobes caused by certain quasi-periodicity of element arrangement while simultaneously maintaining the maximum filling density of the elements. The advantages of the proposed method were analyzed in comparison with the current methods of developing fully populated arrays with a non-regular distribution of elements.

FUNDING

Development of the array design algorithm was supported by the Russian Science Foundation (project no. 19-12-00148). Analysis of the acoustic fields of arrays was supported by the Russian Foundation for Basic Research (project no. 19-02-00035), a stipend from the President of the Russian Federation (SP-2644.2018.4), and a stipend from the Basis Foundation for Development of Theoretical Physics.

REFERENCES

1. L. R. Gavrilov, *Focused High Intensive Ultrasound in Medicine* (Fazis, Moscow, 2013) [in Russian].
2. K. Hynynen and R. M. Jones, Phys. Med. Biol. 61 (17), 206 (2016).
3. W. Kreider, P. V. Yuldashev, O. A. Sapozhnikov, N. Farr, A. Partanen, M. R. Bailey, and V. A. Khokhlova, IEEE Trans. Ultrason., Ferroelectr. Freq. Control 60 (8), 1683 (2013).
4. V. A. Khokhlova, P. V. Yuldashev, P. B. Rosnitskiy, A. D. Maxwell, W. Kreider, M. R. Bailey, and O. A. Sapozhnikov, Phys. Procedia **87**, 132 (2016).
5. G. Pinton, J.-F. Aubry, M. Fink, and M. Tanter, Med. Phys. **38** (3), 1207 (2011).
6. L. Marsac, D. Chauvet, R. La Greca, A.-L. Boch, K. Chaumoitre, M. Tanter, and J.-F. Aubry, Int. J. Hyperthermia **33** (6), 635 (2017).
7. J.-L. Thomas and M. A. Fink, IEEE Trans. Ultrason., Ferroelectr. Freq. Control 43 (6), 1122 (1996).
8. P. B. Rosnitskiy, O. A. Sapozhnikov, H. Grüll, and V. A. Khokhlova, in *Proc. 19th Int. Symp. of ISTU/5th European Symp. of EUFUS* (Barcelona, June 13–15, 2019).
9. D. Cathignol, in *Proc. Nonlinear Acoustics at the Beginning of the 21st Century (2002, Moscow, Russia)* (Moscow State Univ., Moscow, 2002), p. 371.
10. S. Bobkova, L. Gavrilov, V. Khokhlova, A. Shaw, and J. Hand, Ultrasound Med. Biol. **36** (6), 888 (2010).
11. L. R. Gavrilov and J. W. Hand, IEEE Trans. Ultrason., Ferroelectr. Freq. Control **41** (1), 125 (2000).
12. J. W. Hand, A. Shaw, N. Sadhoo, S. Rajagopal, R. J. Dickinson, and L. R. Gavrilov, Phys. Med. Biol. **54** (19), 5675 (2009).
13. S. A. Ilyin, P. V. Yuldashev, V. A. Khokhlova, L. R. Gavrilov, P. B. Rosnitskiy, and O. A. Sapozhnikov, Acoust. Phys. **61** (1), 52 (2015).
14. B. I. Raju, C. S. Hall, and R. Seip, IEEE Trans. Ultrason., Ferroelectr. Freq. Control **58** (5), 944 (2011).
15. P. Ramaekers, M. de Greef, R. Berriet, C. T. W. Moonen, and M. Ries, Phys. Med. Biol. **62** (12), 5021 (2017).
16. P. Ramaekers, M. Ries, C. T. W. Moonen, and M. de Greef, Med. Phys. **44** (3), 1071 (2017).
17. P. B. Rosnitskiy, B. A. Vysokanov, L. R. Gavrilov, O. A. Sapozhnikov, and V. A. Khokhlova, IEEE Trans. Ultrason., Ferroelectr. Freq. Control **65** (4), 630 (2018).
18. S. A. Goss, L. A. Frizell, J. T. Kouzmanoff, J. M. Barich, and J. M. Yang, IEEE Trans. Ultrason., Ferroelectr. Freq. Control **43** (6), 1111 (1996).
19. M. Balzer, T. Schlömer, and O. Deussen, ACM Trans. Graphics (Proc. SIGGRAPH) **28** (3), Article 86 (2009).
20. L. R. Gavrilov, O. A. Sapozhnikov, and V. A. Khokhlova, Bull. Russ. Acad. Sci.: Phys. **79** (10), 1232 (2015).

Translated by N. Podymova